

Analysis of in vitro demineralised human enamel using multi-scale correlative optical and scanning electron microscopy, and high-resolution synchrotron wide-angle X-ray scattering

Besnard, Cyril; Harper, Robert A.; Salvati, Enrico; Moxham, Thomas E.j.; Romano Brandt, León; Landini, Gabriel; Shelton, Richard M.; Korsunsky, Alexander M.

DOI:

[10.1016/j.matdes.2021.109739](https://doi.org/10.1016/j.matdes.2021.109739)

License:

Creative Commons: Attribution (CC BY)

Document Version

Publisher's PDF, also known as Version of record

Citation for published version (Harvard):

Besnard, C, Harper, RA, Salvati, E, Moxham, TEJ, Romano Brandt, L, Landini, G, Shelton, RM & Korsunsky, AM 2021, 'Analysis of in vitro demineralised human enamel using multi-scale correlative optical and scanning electron microscopy, and high-resolution synchrotron wide-angle X-ray scattering', *Materials and Design*, vol. 206, 109739. <https://doi.org/10.1016/j.matdes.2021.109739>

[Link to publication on Research at Birmingham portal](#)

General rights

Unless a licence is specified above, all rights (including copyright and moral rights) in this document are retained by the authors and/or the copyright holders. The express permission of the copyright holder must be obtained for any use of this material other than for purposes permitted by law.

- Users may freely distribute the URL that is used to identify this publication.
- Users may download and/or print one copy of the publication from the University of Birmingham research portal for the purpose of private study or non-commercial research.
- User may use extracts from the document in line with the concept of 'fair dealing' under the Copyright, Designs and Patents Act 1988 (?)
- Users may not further distribute the material nor use it for the purposes of commercial gain.

Where a licence is displayed above, please note the terms and conditions of the licence govern your use of this document.

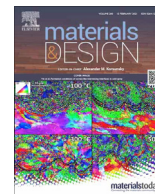
When citing, please reference the published version.

Take down policy

While the University of Birmingham exercises care and attention in making items available there are rare occasions when an item has been uploaded in error or has been deemed to be commercially or otherwise sensitive.

If you believe that this is the case for this document, please contact UBIRA@lists.bham.ac.uk providing details and we will remove access to the work immediately and investigate.

Download date: 18. Apr. 2024



Analysis of *in vitro* demineralised human enamel using multi-scale correlative optical and scanning electron microscopy, and high-resolution synchrotron wide-angle X-ray scattering



Cyril Besnard^{a,*}, Robert A. Harper^b, Enrico Salvati^{a,1}, Thomas E.J. Moxham^{a,c}, León Romano Brandt^a, Gabriel Landini^b, Richard M. Shelton^b, Alexander M. Korsunsky^a

^a MBLEM, Department of Engineering Science, University of Oxford, Parks Road, Oxford, Oxfordshire OX1 3PJ, UK

^b School of Dentistry, University of Birmingham, 5 Mill Pool Way, Edgbaston, Birmingham, West Midlands B5 7EG, UK

^c Diamond Light Source Ltd., Didcot, Oxfordshire OX11 0DE, UK

ARTICLE INFO

Article history:

Received 28 February 2021

Revised 6 April 2021

Accepted 13 April 2021

Available online 23 April 2021

Keywords:

Synchrotron

X-ray diffraction

Enamel

In vitro demineralisation

Scanning electron microscopy

Energy-dispersive X-ray spectroscopy

ABSTRACT

Enamel caries is a highly prevalent worldwide disease that involves the demineralisation of the outer tooth structure. In this study, we report the analysis of artificially demineralised human enamel sections ('slices') etched using lactic acid (2% v/v) in comparison with healthy enamel using correlative techniques of optical and electron microscopy, as well as scanning diffraction. Demineralisation of the enamel was characterised at the micron to sub-micron scale. The structure of the healthy enamel was investigated using Focused Ion Beam - Scanning Electron Microscopy (FIB-SEM) and compared with an etched sample to reveal their structural differences. Additional chemical analysis using energy-dispersive X-ray spectroscopy (EDS) was performed and a decrease in the Ca/P atomic % ratio was found in etched samples in comparison with healthy enamel, suggesting greater loss of calcium compared with phosphorus. Synchrotron wide-angle X-ray scattering (WAXS) was performed on the samples to reveal the differences in the diffraction patterns before and after etching in terms of lattice structure and preferred orientation (texture). Texture maps were extracted from diffraction analysis at 500 nm spatial resolution. These maps were correlated with the dimension of the enamel structure. The multi-scale correlative approach provided insights into the demineralisation-induced enamel structure alteration at a resolution approaching 500 nm.

© 2021 The Authors. Published by Elsevier Ltd. This is an open access article under the CC BY license (<http://creativecommons.org/licenses/by/4.0/>).

1. Introduction

The present study aims to analyse the process of enamel demineralisation after lactic acid exposure by correlating the results acquired from several techniques that can gather data across the enamel hierarchical structure levels, including optical microscopy (mm to μm scale), scanning electron microscopy (SEM) (μm to nm scale), and synchrotron wide-angle X-ray scattering (WAXS) diffraction analysis (μm to \AA scale) to reveal the impact on the crystal structure, morphology and chemical composition.

Enamel caries is a disease that still affects billions of individuals worldwide [1] largely due to the consumption of fermentable sugar and poor hygiene that enable oral bacteria to self-organise in biofilms (dental plaque) producing acid as part of acidogenic bacteria metabolism [2,3]. Enamel consists of a complex arrangement of mineral hydroxyapatite (HAp, 85% by volume [4]), water [5] and a minimal but critical proportion of binding proteins [6]. HAp can be dissolved in the acidic conditions of acidogenic plaque [7–9] resulting in compromised mechanical properties of mineralised dental tissues [10]. Enamel exhibits a hierarchical structure consisting of individual crystallites up to $\sim 100 \mu\text{m}$ in length at the nanometre scale, with average values of 26 nm and 68 nm in terms of width and thickness, respectively [11]. The crystal lattice of HAp in the enamel is hexagonal, belonging to group $P6_3/m$ [12,13]. Enamel HAp displays deviations from the ideal stoichiometry of pure hydroxyapatite $\text{Ca}_{10}(\text{PO}_4)_6(\text{OH})_2$ due to the presence of additional elements, including magnesium (Mg), fluorine (F), sodium (Na) [12,14–18] and carbonate ions [19]. At the microscale enamel

* Corresponding author.

E-mail addresses: cyril.besnard@eng.ox.ac.uk (C. Besnard), R.A.Harper@bham.ac.uk (R.A. Harper), enrico.salvati@uniud.it (E. Salvati), thomas.moxham@eng.ox.ac.uk (T.E.J. Moxham), leon.romanobrandt@eng.ox.ac.uk (L. Romano Brandt), G.Landini@bham.ac.uk (G. Landini), R.M.Shelton@bham.ac.uk (R.M. Shelton), alexander.korsunsky@eng.ox.ac.uk (A.M. Korsunsky).

¹ Present address: Polytechnic Department of Engineering and Architecture, University of Udine, 33100 Udine UD, Italy.

has a prismatic structure containing HAP crystallites oriented with their long dimension predominantly parallel to the longitudinal extent of the enamel rods that are 5–6 μm in diameter [20–23]. This structure arises as a consequence of enamel deposition by ameloblasts [24] during tooth formation (odontogenesis). The detailed arrangement of HAP crystals is not entirely homogeneous, but is characterised by a gradual variation in crystallite orientation [25–28], from top to the bottom of the rods amounting to $\sim 60\text{--}70^\circ$ [25]. Adjacent rods are connected by inter-rod regions described as the sheath [29–32]. At the millimetre scale groups of these rods decussate (intertwine) resulting in an optical contrast effect referred to as Hunter-Schreger bands [33].

The demineralisation process in the enamel is anisotropic due to the non-uniform interaction between the acidic fluid and the multi-scale structures described above, leading to preferential demineralisation elements of enamel structure. Developing effective therapies against enamel dissolution therefore requires a thorough understanding of the structural demineralisation process across the various hierarchical levels. Demineralisation of the enamel (be it under artificial or carious conditions) leads to a decrease in its density [34,35] and was found to result in different patterns at the microscale. Silverstone *et al.* defined three types of etching pattern [36], and later, Galil *et al.* added two more types based on their study using phosphoric acid [37]. In summary, Type 1 corresponds with rod centres being preferentially demineralised, Type 2 with the periphery of rods being preferentially demineralised, and Type 3 is a mixture of Types 1 and 2. Type 4 is characterised by the presence of pits, and Type 5 corresponds with a largely uniform material removal that preserves a relatively smooth surface.

Demineralisation of enamel has been analysed using photography [38], SEM [17,20], X-ray diffraction [39], Fourier transform infrared spectroscopy [39], energy-dispersive X-ray spectroscopy (EDS) [40], Raman spectroscopy [41], X-ray micro-computed tomography [35], radiography [34], optical microscopy [34], atomic force microscopy (AFM) [42–45], transmission electron microscopy (TEM) [46], and atom probe tomography [16]. Results from such analyses and observations of demineralisation led to attempts to understand the underlying origins of the demineralisation process and its progress using modelling [17,47,48].

In addition to laboratory analysis, synchrotron X-ray experiments have been used to elucidate changes in the structure of the demineralised region. Another technique used to examine this was WAXS that revealed modification of the enamel structure during *in situ* and *ex situ* experiments of enamel (carious, non-carious and artificially demineralised), although the resolution used ($\geq 20 \mu\text{m}$) was larger than the nano- and micro-scale features present in the enamel [49,50]. In the most advanced studies resolution has been improved down to 500 nm for healthy enamel in the research by Free *et al.* on TEM lamella [51].

WAXS has been used extensively to obtain information regarding the properties of polycrystals such as lattice distortion and preferred orientation (texture). Appendix Table A.1 provides a non-exhaustive list of the studies on teeth with the corresponding resolution reported.

To date there appears to be no research published using transmission WAXS at sub-micron resolution over a thickness greater than very thin ($\sim 1 \mu\text{m}$) TEM lamella performed on sound and etched enamel. Kirkpatrick-Baez (KB) X-ray mirrors can be used to attain this high spatial resolution in synchrotron experiments. The method was previously applied to analyse dental tissues affected with erythroblastosis fetalis [52] and also for fluorescence analysis of teeth [53]. In another study, high-resolution of 500x500 nm was achieved over an area of $\sim 11 \times 20 \mu\text{m}^2$ [51], allowing sub-micron mapping of healthy enamel rods.

2. Method – Materials

2.1. Sample preparation and ethical information

Four 100 μm slices of human dental enamel from two human third molar teeth (extracted for non-carries-related therapeutic reasons) were produced by cutting using a 4-inch diameter low speed diamond wafering saw (Buehler IsoMet[®], U.K.) followed by whetstone polishing. The experimental procedure was approved by the National Research Ethics Committee; NHS-REC reference 14/EM/1128/ Consortium Reference BCHDent332.1531.TB. Cutting the samples generated a random selection of rod orientations to explore the effect of orientation on the etching type. To exclude the surface aprismatic enamel the first 100 μm cuts were discarded, the next two further cuts produced the control sample and then the sample to be exposed to acid. Sample 1 (S1, reference) was untreated enamel, sample 2 (S2) was a neighbouring slice etched by immersion in 2% (v/v) lactic acid for 2 h. Lactic acid was selected because it is produced in cariogenic biofilms and the concentration (2%) was selected in order to generate substantial etching during the beamtime allocated. Samples 3 and 4 (S3 and S4) were processed in the same manner as S1 and S2. It is important to note that the slices were immersed in acid and therefore subsurface enamel was exposed to the bulk acid, which would not occur *in vivo*. The slices were rinsed with water and stored in phosphate-buffered saline solution for transport. A schematic of the sample preparation procedure is shown in Fig. 1.

2.2. Synchrotron WAXS

2.2.1. Setup

WAXS experiments were carried out at the Diamond Light Source, Oxford Harwell Campus, Didcot, U.K., on beamline B16 [54] using X-ray beam energy of 18 keV equivalent to the wavelength of 0.6888 Å. The setup is shown in Fig. 2a. A pair of KB mirrors were used to obtain a $0.5 \times 0.5 \mu\text{m}^2$ beam spot on the sample by

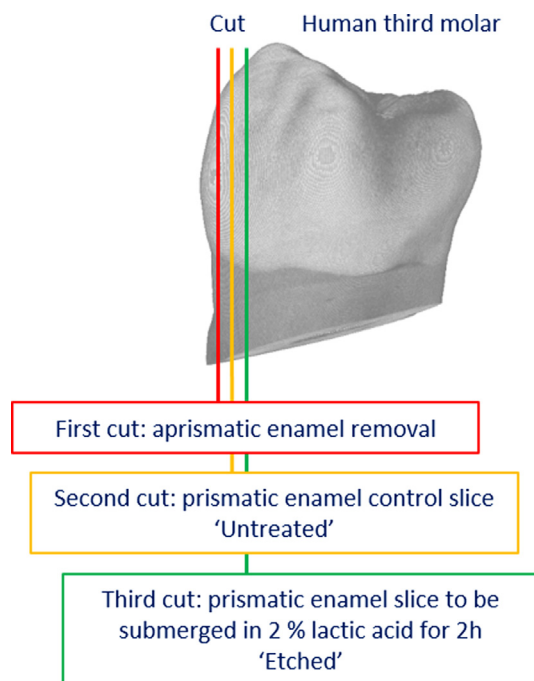


Fig. 1. Schematic diagram of cutting for sample preparation. Each cut is taken at 100 μm depth.

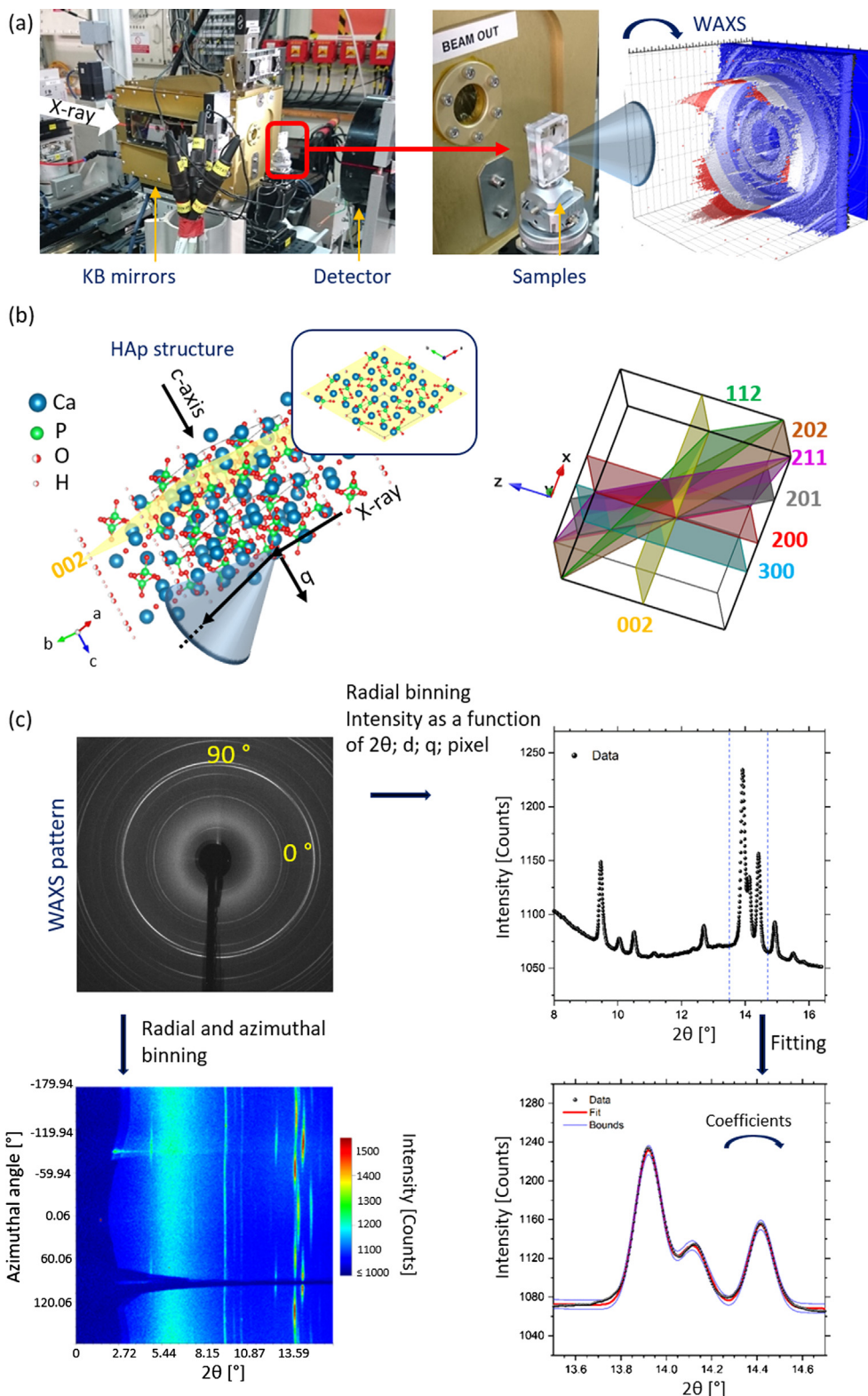


Fig. 2. WAXS setup used on beamline B16 and crystal structure analysis from diffraction. (a) Photographs of the setup of the synchrotron experiment for the WAXS scan with the position of the samples and detector and the illustrations of Debye-Scherrer rings of one acquisition and (b) the resume of the analysis from the WAXS pattern. The crystal structure obtained with VESTA [56] and CrystalMaker® (CrystalMaker Software Ltd, Oxford, England) from cif file 203027 ICSD [57], with the highlight of a few planes. (c) The schematic of the process for analysing the WAXS pattern is illustrated. The process started from the crystal structure shown in (b) and then continued with the diffraction of the lattice planes. From the WAXS pattern produced, binning was performed radially to obtain a 1D plot of intensity as a function of 2θ and then this was fitted to compute coefficients. Radial and azimuthal binning was also performed.

horizontal and vertical focusing [55]. The detector used to record WAXS diffraction patterns was Image Star 9000 (Photonic Science

Ltd, U.K.) with 3056x3056 pixels matrix (pixel size: 31 μm). Each sample was positioned on the stage that could be translated

in x and y (horizontally and vertically across the beam) and z (along the beam) directions, as well as tilted. For each sample, a map of $\sim 10 \times 10 \mu\text{m}^2$ area was acquired with a step of $0.5 \mu\text{m}$ (441 images per sample). For each diffraction image acquired, two minutes exposure was used. All tests were conducted at room temperature.

2.2.2. WAXS analysis

WAXS was carried out to obtain details on the structure of the enamel and on the texture, based on the diffraction by the crystal lattice.

Each WAXS pattern was an acquired image featuring Debye-Scherrer rings that provided information on intensity versus interplanar spacing and which correlated with the sample structure according to Bragg's Law [58], a fundamental expression in diffraction theory [59], where the interplanar spacing is d (in Å):

$$n\lambda = 2d_{hkl} \sin \theta \quad (1)$$

where n indicates an integer of wavelength, λ is the wavelength in Å, hkl are the Miller indices and θ is half of the scattering angle in radians.

The rings had different intensities and widths which related to the structure of the sample (in this case HAp in a non-ideal structure) and were correlated with the plane of the crystal structure. The image processing of the pattern was carried out using ImageJ/Fiji [60,61], and the data analysis program DAWN Science (version 2.11.0) being a Data Analysis Workbench [62,63]. The WAXS calibration was done using standard lanthanum hexaboride (LaB_6) from a National Institute of Standards and Technology (NIST). The calibration was done without KB mirrors due to the lack of signal. By doing this, the beam centre from the calibration was changed and the beam centre was found from the sample itself using a Debye-Scherrer ring, which was fitted using DAWN Science.

The radial-azimuthal binning of the WAXS patterns to obtain a one-dimensional (1D) plot of intensity (I) versus scattering angle 2θ (or d or q scattering vector or pixel) was carried by processing the data from selected pattern sectors into 1D profiles in the procedure specified by the user [64,65]. Considering the large number of two-dimensional (2D) diffraction patterns acquired, a processing list was applied within DAWN Science software that allowed automatic exporting of 1D radial plots. Each azimuthal binning angle required setting up a radial range, radial bin selection, azimuthal range and calibration file. For an azimuthal binning with a centre of 0° , the azimuthal angle was selected from -10 to 10° with a radial binning of 3000 bins. A combination of in-house developed Matlab (MathWorks, USA) scripts and 'Generate Script' and 'Generate Code' (from Matlab) were used to import and process the data for further analyses.

WAXS provides information on crystal structure and composition. The patterns obtained were compared with a hydroxyapatite structure from the crystallography open database (COD) [66] file 9001233 (DIFFRAC.EVA software Bruker AXS GmbH, Karlsruhe, Germany, COD Database and cif file 203027 from ICSD [57,67]).

To analyse the 1D plot of intensity (I) versus scattering angle 2θ for each pattern, a Gaussian function [65,68] was used to fit single peaks using (cftool, Matlab) and to extract the information related to the peaks (e.g. position, and amplitude), using Eq. (2):

$$Y = Ae^{-\frac{(x-c)^2}{2w^2}} + B + sx \quad (2)$$

where x is the scattering angle 2θ ; A is the peak amplitude; c is the peak centre; w is the Gaussian peak width; B is the background intensity, and s its slope.

For the analysis of multiple peaks, a sum of Gaussian functions was used and deconvolution of each peak's contribution was carried out by refining the parameters in the Eq. (3):

$$Y = B + sx + \sum_{k=1}^n A_k e^{-\frac{(x-c_k)^2}{2w_k^2}} \quad (3)$$

where n is the maximum number of peaks, and k is the index.

Following the fitting of intensity as a function of 2θ , the lattice spacing d of each peak can be determined from Bragg's law as:

$$d_{hkl} = \lambda / 2 \sin \theta \quad (4)$$

The ratio of specific peak intensities provides information about the sample texture. Azimuthal binning was performed in the azimuthal angle range from 0 to 360° , and the texture was evaluated from the relative intensity of (2 1 1) and (3 0 0) peaks using the texture index $R = (I_{211}/I_{300})/Cst$ in accordance with previous publications [69,70]. Here Cst is the ratio of the two intensities from a sample with random orientation, set to $st = \frac{I_{211}}{I_{300}} = 1.63$. This analysis was performed on each WAXS pattern collected. A review of the texture index measurement on HAp and teeth is provide in Appendix Table A.2.

Using the software DAWN (process 'cake remapping') binning was carried out along the radial and azimuthal angles of the WAXS patterns. The number of bins was 3000 for both axes, and the azimuthal angle ranged from -180° to 180° . The main steps in the procedure are shown in Fig. 2b.

The resulting 1D diffraction patterns, Debye-Scherrer rings, and R index maps were visualised using Matlab and OriginPro v2019b (OriginLab Corporation, Northampton, MA, USA).

2.3. Microscopy

Samples were observed using a polarising light microscope, Promotech (Zeiss, Germany), equipped with a quarter wave plate compensator.

Each sample was subsequently analysed using a SEM Tescan Lyra 3 (Tescan, Czech Republic) with secondary and backscattered electron imaging (SEi and BSi respectively) using a voltage from 3 keV to 10 keV. Samples were coated with gold (Au) and palladium (Pd) with a thickness of ~ 5 nm using SC7620 sputter coater (Quorum Technologies, U.K.), and silver paint was applied on the side of the samples to ensure conduction with the mounting holder. Focused ion beam (FIB) – SEM was carried out on S3 and S4 using a gallium (Ga) ion beam at 30 keV. The FIB analysis was performed in 4 steps, with deposition of platinum, milling and thinning and a marker was placed for drift corrections during the analysis, all implemented in Lyra software. The three-dimensional (3D) reconstruction was done using Avizo v2020-1 software (Thermo Fisher Scientific, USA) [71], the image slices were filtered with a median filter, aligned and manually segmented to extract the rod using mainly the presumed inter-rod structure. The voxel size was ~ 29 nm. The elemental analysis was acquired using an Xmax 150 EDS detector and Aztec Oxford Instruments software (Oxford Instruments, U.K.) with a voltage of 10 keV using the same time of acquisition, process and number of channels to standardise the measurements. Quantification of the ratio of calcium/phosphorus (Ca/P) atomic (%) was done using Aztec, using Ca (emission line $K_{\alpha 1} = 3691.68$ eV) and P ($K_{\alpha 1} = 2013.7$ eV) [72].

The simulation of the interaction volume of the electron from SEM analysis was carried out using CASINO software v2.51 64bits [73] to predict the volume involved in the EDS acquisition. The material needs to be defined and here two cases were considered, with $\text{Ca}_{10}(\text{PO}_4)_6(\text{OH})_2$ selected (ideal HAp structure) as a substrate with either a density of $2.42 \text{ g}\cdot\text{cm}^{-3}$ for untreated or a density of

$1.26 \text{ g}\cdot\text{cm}^{-3}$ for demineralised enamel. For the density of untreated material, an average of some measurements from sound enamel and for the treated material, the minimum value measured on a lesion from the study on white spot enamel lesion of Cochrane *et al.* [74]. The set up for the calculation of the interaction volume used the following parameters: 10,000 electrons simulated, a beam radius of 7.1 nm, at beam energy of 10 keV and the detector geometry. Coating of Au/Pd with a thickness of 5 nm was also implemented in the material defined. The interaction volume calculated was below the diameter of the rod. For density of $2.42 \text{ g}\cdot\text{cm}^{-3}$, around $1.1 \mu\text{m}$ in depth and $0.9 \mu\text{m}$ in radius and for density $1.26 \text{ g}\cdot\text{cm}^{-3}$, the values were 2.2 and $1.8 \mu\text{m}$ respectively following prediction using CASINO simulation (Appendix Fig. A.1).

2.4. Statistics analysis

One-way ANOVA with post hoc Tukey's test was performed on the EDS analysis of the atomic (at.) % of the ratio of Ca/P (at. %) and on the R index using OriginPro. A value of $p < 0.05$ was considered statistically significant. In the Figures, the * mark corresponds to $p < 0.05$.

3. Results and discussion

3.1. Microscopy analysis

The transmitted polarised light images of the samples before etching (Fig. 3), clearly showed Hunter-Schreger bands. The etching removed the birefringence from the enamel as observed in the carious or artificially etched samples [34,75,76].

To further elucidate the surface modification arising from etching at higher magnification and resolution, SEi and BSi analysis were carried out on area representative of the hierarchical structure of enamel. After etching, the two samples demonstrated preferential demineralisation in the enamel (Fig. 4) similar to previous reports on enamel [20,49]. To confirm these features, the untreated enamel was examined using SEM and no clear rod or inter-rod was observed in either case (Appendix Fig. A.2). The rod orientations in several locations of S3 was revealed using FIB-SEM, and shown in two-dimension and three-dimension (Appendix Figs. A.3, 4), however the crystallites could not be identified. Rods were suggested by the absence of material in what appeared to be the inter-rod region as shown in Appendix Fig. A.4. This may arise as a consequence of the thinning process potentially generating a polished or near-polished surface on the enamel cross-section which revealed a boundary from lateral etching of the Ga ions [77,78].

A difference in the orientation of the rods was observed in the two etched samples. In S2, rods were more longitudinally aligned than in S4, being more transversally oriented in certain locations. This difference in orientation led to different types of demineralisation with a Type 2 etching pattern in S2 and demineralisation occurring within the inter-rod zone, whilst for S4, etching patterns Type 1–2–3 were observed. The demineralisation of the rod core was observed in some locations of S4 with a cavity in the middle of the rods, Fig. 4. Additionally FIB-SEM analysis of S4 showed demineralisation below the surface revealing porosity in rods and a complex demineralisation of the enamel at a different scale: from rod to inter-rod but also between individual crystallites (Appendix Fig. A.5), similar to the SEM analysis of etched enamel reported by DeRocher *et al.* [17].

It was interesting that the etching patterns were different in the two etched samples. This could be have been due to the different orientation of the slices during sample preparation, similar to the observations by Risnes and Li [20]. Previously, it was found that

for longitudinal cuts, the inter-rod region was preferentially affected after exposure to acid using hydroxyethyl cellulose and lactic acid [79]. In other studies, also using lactic acid, the core was found demineralised with the sample orientation suggested to be more transverse than longitudinal [49,80] from the SEM images shown. The etching observations of the present study are in agreement with the work from Silverstone *et al.* [36] who reported difficulty assigning a type of etching pattern to a particular acid.

3.2. Elemental analysis

While the surface of the enamel was shown to be modified from the optical microscopy and scanning electron microscopy analysis, it was important to examine whether the chemistry was also modified. The chemical changes were examined using EDS elemental analysis (representative EDS spectra are displayed in Fig. 5a). Ca and P in hydroxyapatite were found, which was consistent with what has been previously reported in enamel [81]. The coating necessary for SEM analysis also contributed to the intensities of the Au and Pd peaks. Following the quantification of each spectrum acquired, the variation of the Ca/P ratio was assessed based on respective at. %. The Ca/P ratios of S1–S2–S3–S4 were 1.44 ± 0.096 , 1.19 ± 0.29 , 1.49 ± 0.053 and 1.09 ± 0.28 respectively, while stoichiometric HAp has an atomic ratio of 1.67. Data from multiple locations indicated a more dispersed Ca/P ratio present in the etched samples compared with the untreated samples and there was a significant difference between each untreated and treated sample (Fig. 5b). The decrease in Ca/P ratio was suggested to correlate with a preferential decrease in the calcium content instead of the changes in the phosphorus content. The decrease in the Ca/P ratios observed after demineralisation closely matched results described previously as summarised in Appendix Table A.3.

3.3. WAXS

The representation of the Debye-Scherrer rings in each sample is shown in Fig. 6 with rings correlated with a set of the (*hkl*) planes satisfying Bragg's law. The plane indexing in each sample showed a very low intensity for the (0 0 2) plane. This plane is commonly used for determining the orientation of the crystallite and crystallite length based on databases such as COD 9001233 and cif files [49]. Overall, a discontinuity in some rings demonstrated the presence of texture [82] and the observation of sharp rings confirmed the crystallinity of the samples [83]. This was also observed in the plots after radial and azimuthal binning. From the intensity of each WAXS pattern, clear differences could be observed between S1 (intact enamel with high intensity for the peaks at high angle) and S2 (etched enamel). For S3 and S4, the intensity at a low angle was higher in the intact enamel compared with the etched sample, but similar to S1, where preferential orientation after etching could be observed from the difference in the WAXS ring patterns.

After azimuthal binning with a centre angle of 0° and post azimuthal binning, the 441 files of each image were plotted to study the intensity versus the angle 2θ (Fig. 7). In all four samples, the hydroxyapatite patterns closely matched the database considering a shift in *d* spacing. It is worth noting that the database used was from an apatite sample and not from human enamel, which could explain the shift of the data [57].

As shown in Fig. 7, the difference in the distributions of the intensity of the reflections before and after etching, might have implied that demineralisation was not homogeneous and preferential etching occurred. Interestingly, the patterns of the two intact enamel pieces were significantly different, where S1 showed a clear reflection of the (1 1 2) peak while S3 had a significantly higher intensity for (2 0 0) peak. In S4, overall there was a low

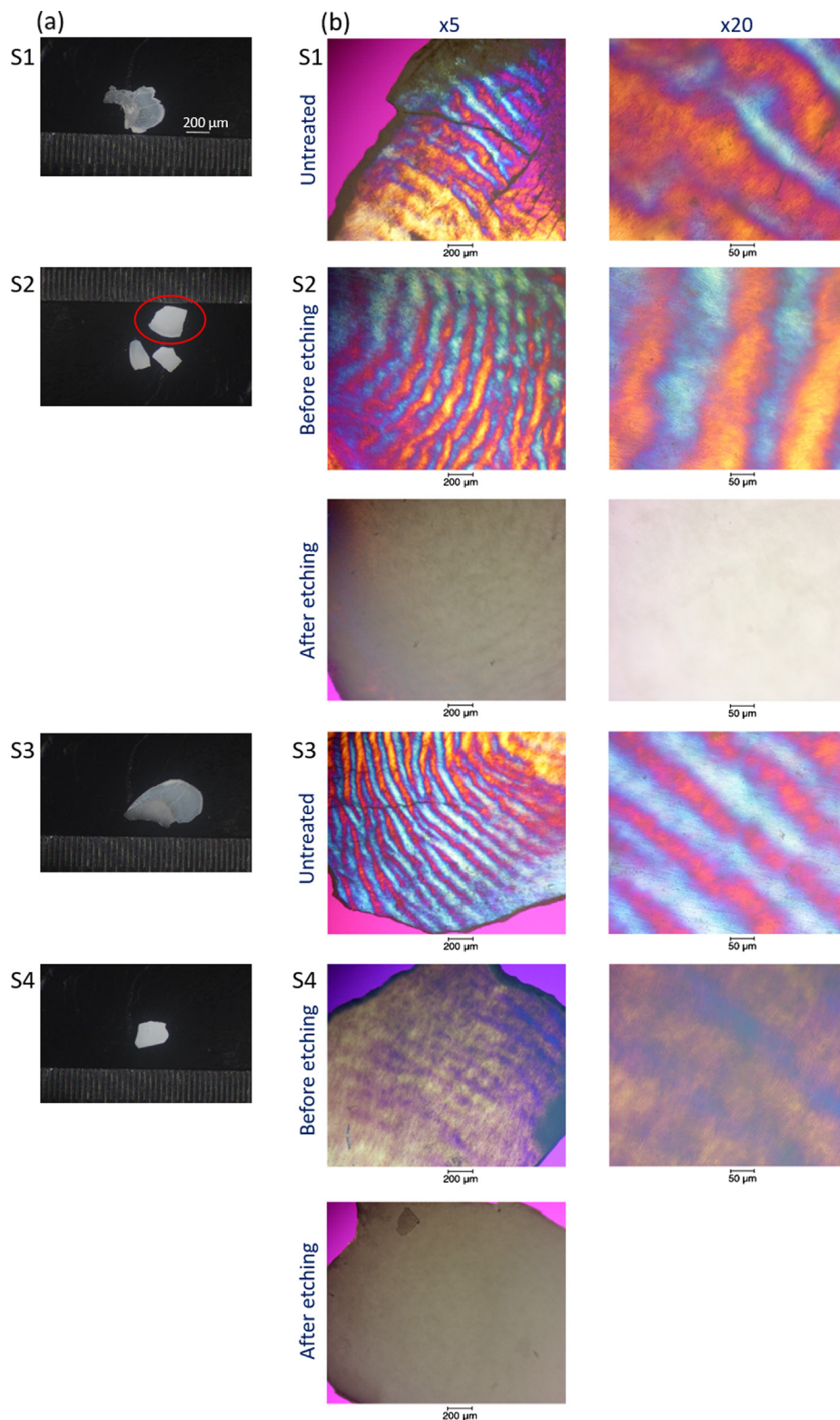


Fig. 3. View of the four samples and optical microscopy analysis. For each sample (a) photographs and (b) transmitted polarised light images are presented. For S2 and S4, the images before and after etching are shown. Images were captured with x5 and x20 objectives.

intensity in the (2 0 0) peak, which suggested that this plane was modified after etching, there are not many publications highlighting the changes in the (2 0 0) peak and this shall be investigated further in future studies. For the (0 0 2) peak, the details were reported in [Appendix Note 1](#).

Beyond the angle 0°, the evolution of the 1D profile was carried out by radial-azimuthal binning with the centre angle from -40° to 140° 2θ. [Fig. 8](#) shows the individual diffractograms before and after etching and with the stacking results for two angles (for an azimuthal step of 10° see [Appendix Fig. A.10](#)). Each sample revealed

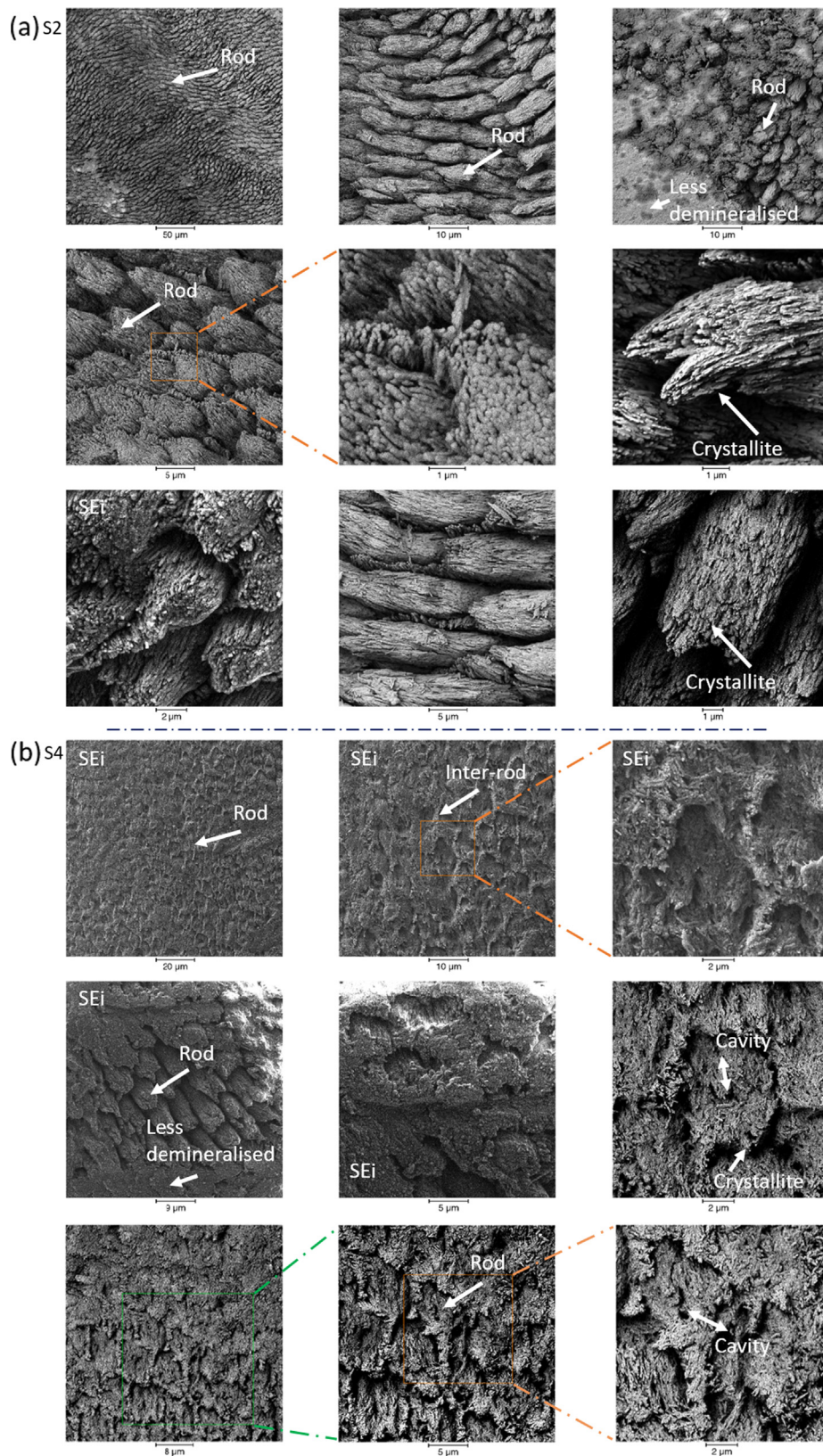


Fig. 4. SEM analysis of the two etched samples, S2 and S4, revealing the different demineralised microstructure. SEi or BSi of (a) S2 and (b) S4 acquired in several locations showed the difference in rod orientations in the enamel, see the first row of both samples. With higher magnification, rods and inter-rods were clearly observed, and with even higher magnification, the crystallites could be identified. Cavities were also observed in S4 (double arrows) in the centre of the rods, less demineralised than inter-rods. Less demineralised regions are also highlighted in both samples in the figure.

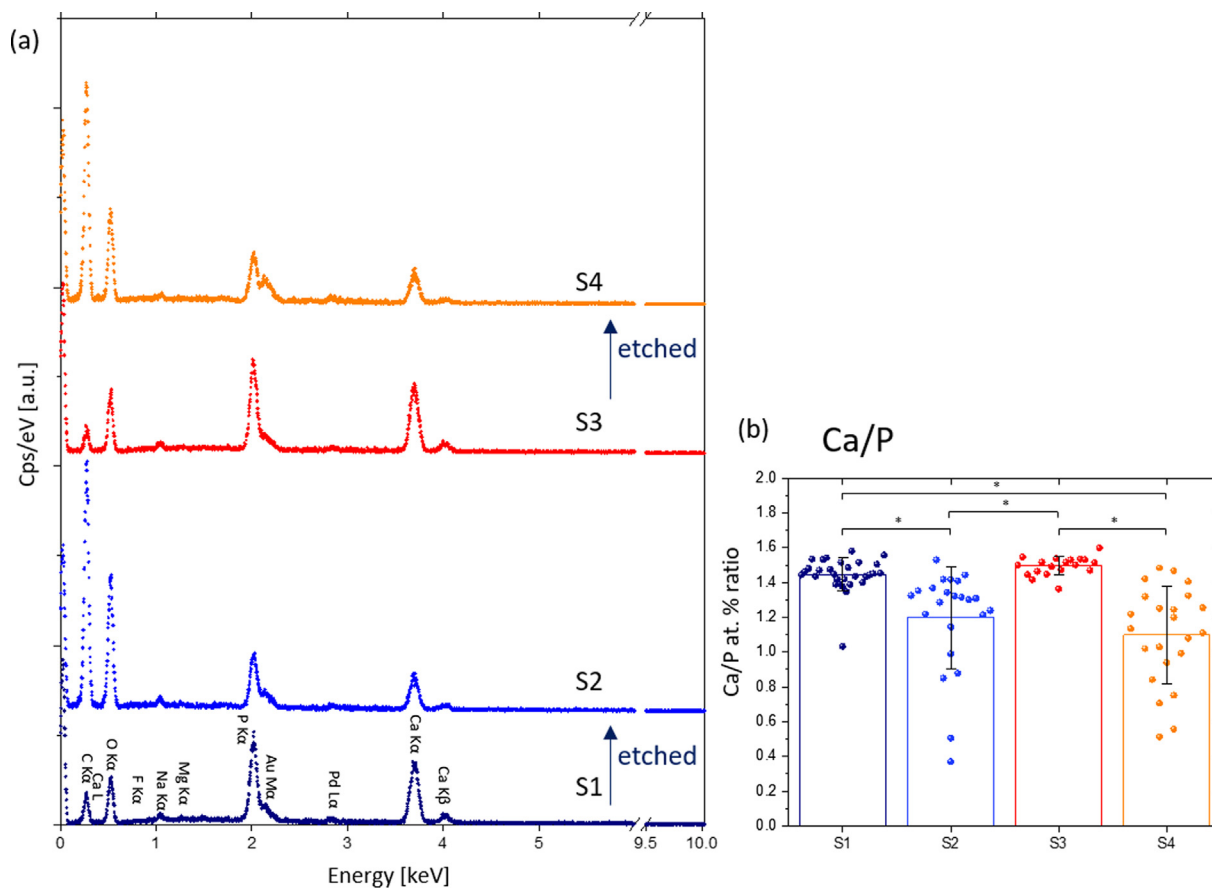


Fig. 5. SEM-EDS analysis of the four samples on the Ca/P at. % ratio. (a) Stack of the EDS spectra from a location of each samples detecting Ca and P elements with emission lines $K\alpha$ (~ 3.7 and 2 keV respectively). (b) The bar graph showing the mean and the standard deviation of Ca/P at. % ratio from several locations of the samples and the statistic results from one-way ANOVA test. * <0.05 used for statistical significance.

a texture (Fig. 8) confirming modifications of the patterns according to the angle 2θ . Analysis of the peaks demonstrated differences in the diffractograms revealing a modification of the crystal structure at the lattice scale after etching. For S1, the $(2\ 0\ 0)$ peak contributed less to the high angle (in the range of angle acquired) in comparison with S2.

In S3 the intensity of the $(2\ 0\ 0)$ peak was detected in several locations and the peak intensity was less prominent after etching. A low intensity of the $(0\ 0\ 2)$ peak was observed in both S3 and S4, revealing the orientation of the samples. The intensities in the high angle with the reflection of $(2\ 1\ 1)$, $(1\ 1\ 2)$, $(3\ 0\ 0)$ and $(2\ 0\ 2)$ peaks were different in the two samples confirming the changes in lattice. Based on the diffractograms, intact and the etched enamel had different structure.

The R index (defined in the method) was analysed and the four samples showed significant differences in their R values (ANOVA on the analysed 441 locations, Fig. 9a). The R index was rendered as a 2D map (Fig. 9b). The analysis of the R index (Fig. 9) revealed a texture at several locations with $R > 1$ and $R < 1$ (where $R = 1$ means random orientation). Values of $R < 1$ were commonly observed in S2 whereas $R > 1.05$ was observed in S1. For S3 and S4, R index increased after etching. Clusters of close values of R index were present in S2, S3 and S4 and it is proposed that these features correlated with rod structure as a consequence of similar dimensions.

Previously, Siddiqui *et al.* analysed the $(0\ 0\ 2)$ plane [50] and reported a loss of texture after demineralisation compared with healthy enamel. However, there were no X-ray diffraction pattern comparisons with other planes. Yang *et al.* studied the R index with

the ratio of the intensity of the $(0\ 0\ 2)$ and $(2\ 1\ 1)$ peaks and found an increase in texture after acid etching [84]. An increase in alignment was also reported during *in situ* demineralisation of enamel [49], however, there was no significant modification observed in the alignment of crystallites in carious regions. A decrease in full width at half-maximum following small-angle X-ray scattering analysis was, however, noticed [85].

4. Conclusions

Four enamel samples were analysed using a combination of various techniques. Optical microscopy, demonstrated the effects the acid demineralisation of the enamel reduced the birefringence and hence was used to identify demineralised enamel. This loss of birefringence was correlated at the micron scale using SEM that demonstrated clear demineralised regions, with porosities both within rods as well as inter-rods. FIB-SEM revealed the rod structure in normal enamel but also highlighted the difficulty identifying crystallites, which could be seen in etched samples. Changes in enamel structure were also correlated with EDS analysis where a significant decrease in the Ca/P ratio was found after acid etching showing a preferential loss of Ca compared with P. This modification in chemistry and structure was correlated with changes in the crystal structure detected by WAXS analysis which showed (at the lattice scale within the sub-micron region) the presence of texture in all the four samples. The differences in diffractograms were found to be correlated with the modification in the crystal lattice. A significant decrease in the intensity of the $(2\ 0\ 0)$ peak was found in S4 compared with S3 demonstrating preferentially modifica-

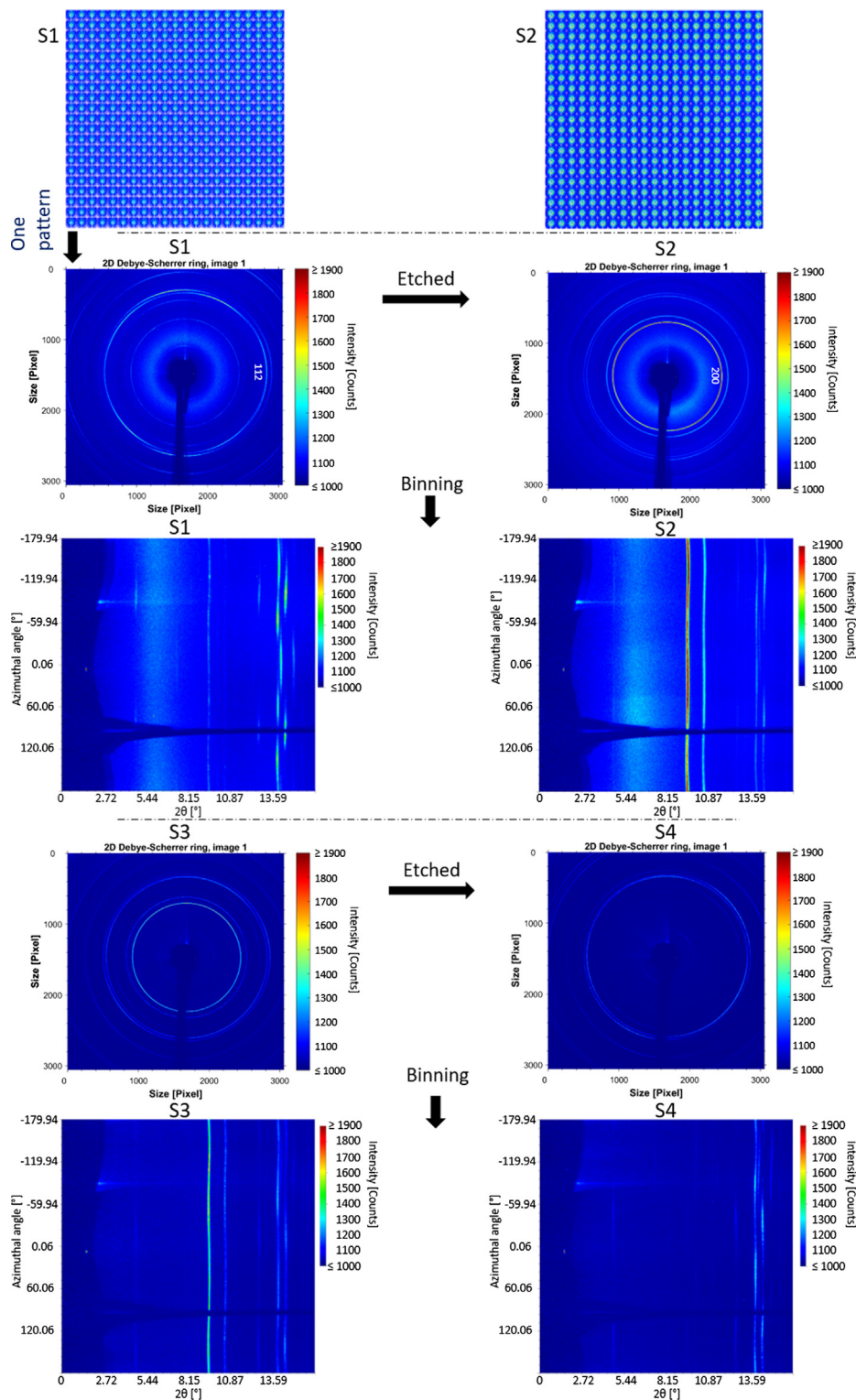


Fig. 6. Illustration of the WAXS pattern from each sample and the radial and azimuthal binning from the same pattern. WAXS patterns show the Debye-Scherrer rings of each sample with the plot after radial and azimuthal binning. For S1, full datasets shown. The colour maps represent intensities.

tions of this plane after etching. From the R index analysis, the sub-region with dimensions similar to the rod or inter-rod structure could be observed in S2, S3 and S4, showing the potential of this technique to analyse down to the resolution of 500 nm after acid

etching. This work extended our knowledge of the changes occurring at the micro to sub-micron range, and highlights the need of high-resolution to identify any changes at the rod and inter-rod level.

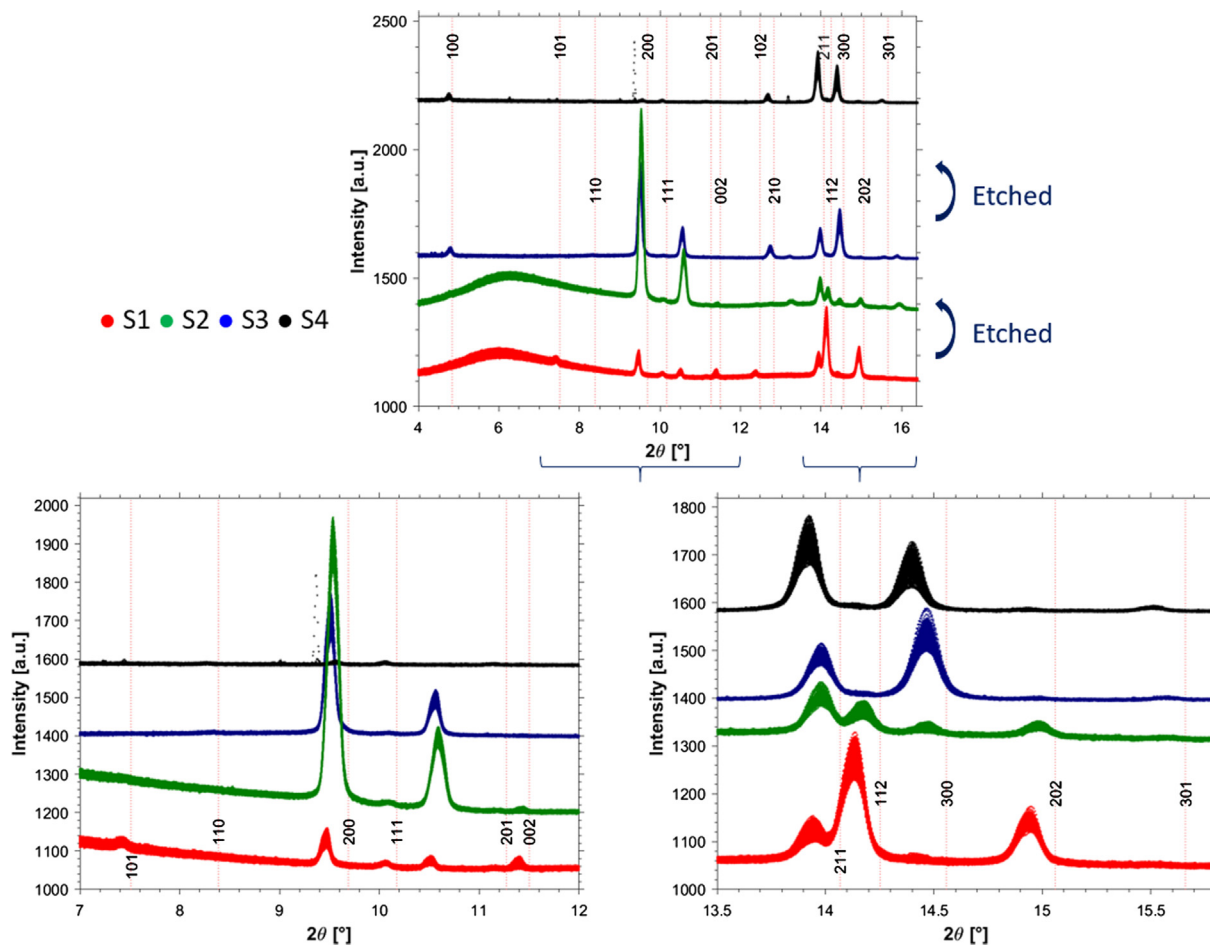


Fig. 7. Diffractogram from each location of the four samples after radial-azimuthal binning centre at 0°. Stack of 1D profile diffractograms of each sample after radial-azimuthal binning from an azimuthal angle centre at 0°, and the zoom of 2 range of 2θ. In Appendix Fig. A.6, radial plot for each location analysed is illustrated with colour maps used to visualise the intensity, and in the Appendix Fig. A.7, the intensity of the pattern of the four samples was plotted as a function of the d spacing.

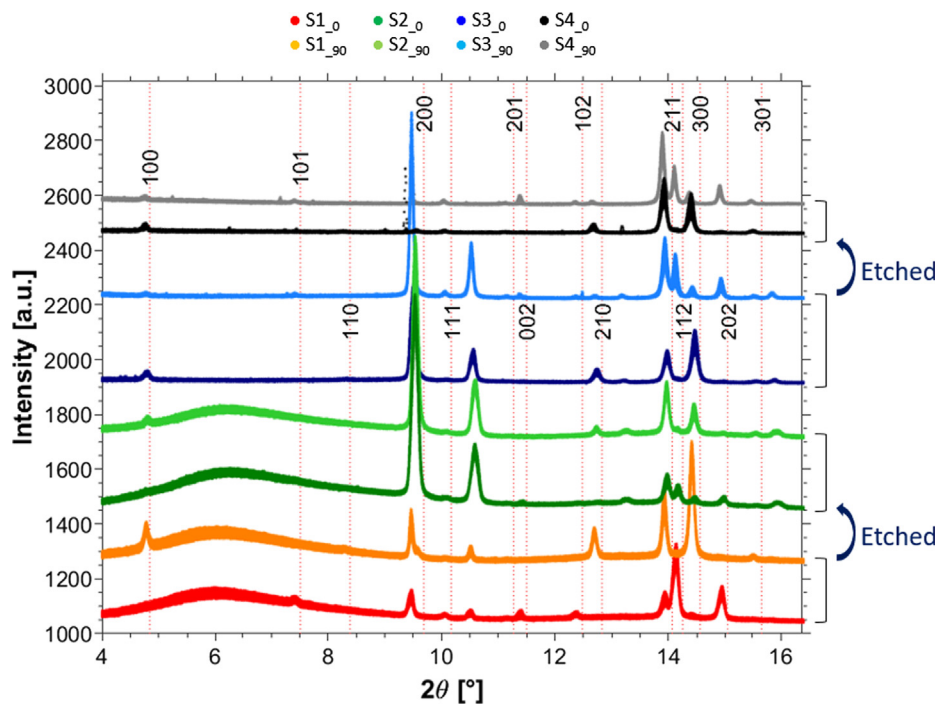


Fig. 8. Analysis of the diffractogram of the four samples at different angles. Stack of 1D profile diffractograms after radial-azimuthal binning centre at 0 and 90° for the four samples. Additional angles are illustrated in Appendix Fig. A.10.

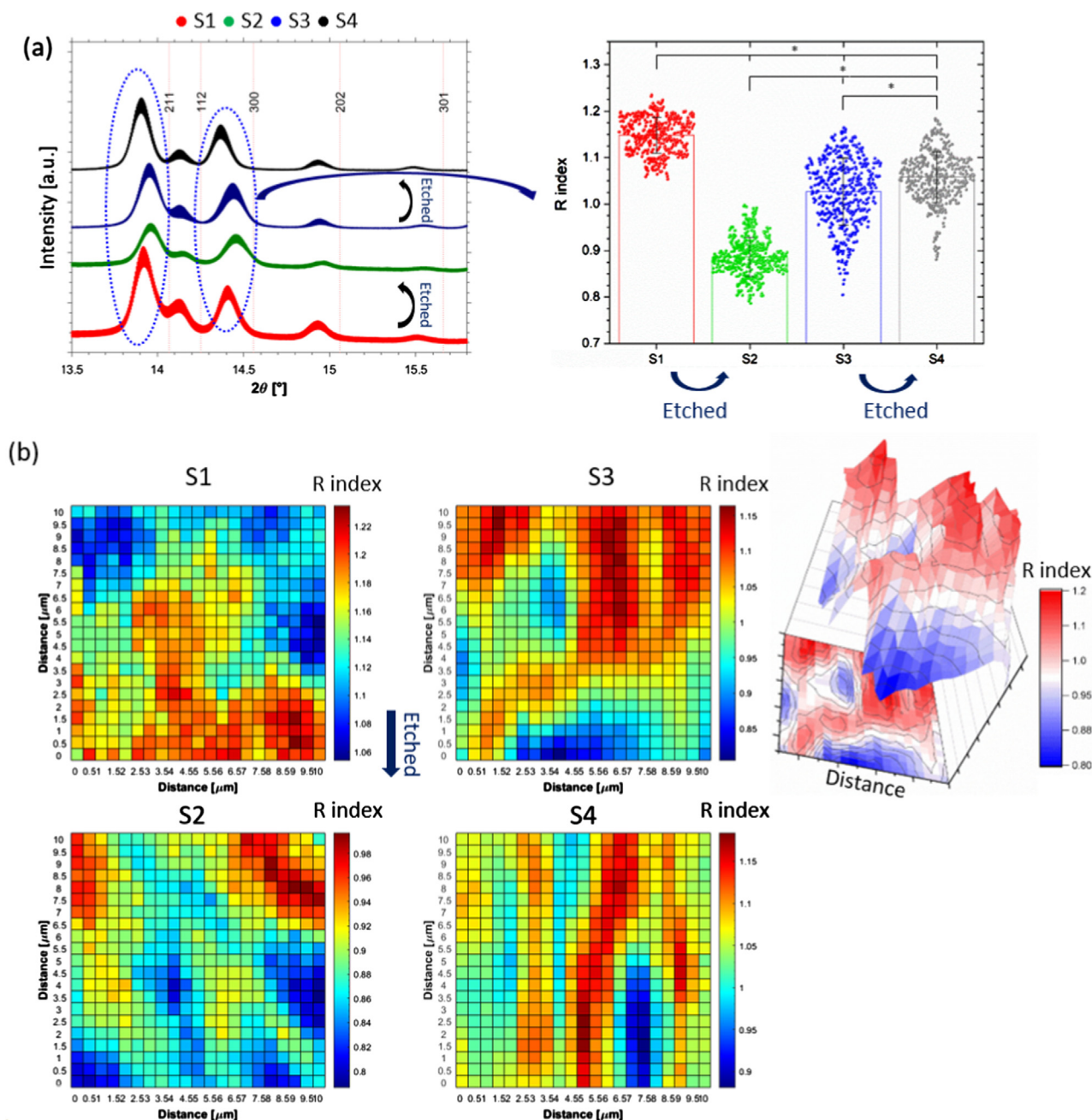


Fig. 9. Analysis of the texture index of the four samples in each location analysed. (a) Plot of intensity as a function of 2θ from 13.5 to 15.8° for the 4 samples from 0 to 360° radial-azimuthal binning (for larger range of 2θ , Appendix Fig. A.11), and plot of each R index. Statistics results from one-way ANOVA test. * <0.05 used for statistical significance. Fitting for one location of each sample in Appendix Fig. A.12. (b) R index map for each sample with addition of 3D representation for S3 and contour (0.361 increment) to highlight the presence of clusters.

Data availability statement

Data collected and interpreted in this study is maintained by the authors and can be made available upon request.

Declaration of Competing Interest

The authors declare that they have no known competing financial interests or personal relationships that could have appeared to influence the work reported in this paper.

Acknowledgements

This work was funded by The Engineering and Physical Sciences Research Council (EPSRC) entitled “Tackling human dental caries by multi-modal correlative microscopy and multi-physics modelling” (EP/P005381/1). The access to Diamond Light Source was under the proposal MT21419-1. Thanks to Diamond Light Source and particularly the team of B16 Dr. Igor Dolbnya and Dr. Oliver Fox, for beamline support and Dr. Jacob Filik for his support with the DAWN software. Thanks to Dr. Jonathan D. James (School of Dentistry, University of Birmingham) for support with preparation

of the samples and optical imaging. Thanks to Petr Buček (Tescan, U.K.) for support with FIB-SEM and Dr. Marzena Tkaczyk (Laboratory for In-situ Microscopy & Analysis, University of Oxford, U.K.) for support with sample coating.

Appendix A. Supplementary material

Supplementary data to this article can be found online at <https://doi.org/10.1016/j.matdes.2021.109739>.

References

- S.L. James et al., Global, regional, and national incidence, prevalence, and years lived with disability for 354 diseases and injuries for 195 countries and territories, 1990–2017: a systematic analysis for the Global Burden of Disease Study 2017, *The Lancet* 392 (2018) 1789–1858, [https://doi.org/10.1016/S0140-6736\(18\)32279-7](https://doi.org/10.1016/S0140-6736(18)32279-7).
- R. Matsui, D. Cvitkovich, Acid tolerance mechanisms utilized by *Streptococcus mutans*, *Future Microbiol.* 5 (2010) 403–417, <https://doi.org/10.2217/fmb.09.129>.
- P.D. Marsh, A. Moter, D.A. Devine, Dental plaque biofilms: communities, conflict and control, *Periodontology* 2000 (55) (2011) 16–35, <https://doi.org/10.1111/j.1600-0757.2009.00339.x>.
- J.D.B. Featherstone, A. Lussi, Understanding the chemistry of dental erosion, *Monogr. Oral Sci.* 20 (2006) 66–76, <https://doi.org/10.1159/000093351>.
- E. Bonte, N. Deschamps, M. Goldberg, V. Vernois, Quantification of free water in human dental enamel, *J. Dent. Res.* 67 (1988) 880–882, <https://doi.org/10.1177/00220345880670051701>.
- T. Baumann, T.S. Carvalho, A. Lussi, The effect of enamel proteins on erosion, *Sci. Rep.* 5 (2015) 15194, <https://doi.org/10.1038/srep15194>.
- D. Kim et al., Spatial mapping of polymicrobial communities reveals a precise biogeography associated with human dental caries, *Proc. Natl. Acad. Sci.* 201919099 (2020) 2020, <https://doi.org/10.1073/pnas.1919099117>.
- W.J. Loesche, Role of *Streptococcus mutans* in human dental decay, *Microbiol. Rev.* 50 (1986) 353–380.
- J.D.B. Featherstone, The science and practice of caries prevention, *J. Am. Dental Assoc.* 131 (2000) 887–899, <https://doi.org/10.14219/jada.archive.2000.0307>.
- T.T.Y. Huang, L.H. He, M.A. Darendeliler, M.V. Swain, Nano-indentation characterisation of natural carious white spot lesions, *Caries Res.* 44 (2010) 101–107, <https://doi.org/10.1159/000286214>.
- G. Daculsi, J. Menanteau, L.M. Kerebel, D. Mitre, Length and shape of enamel crystals, *Calcif. Tissue Int.* 36 (1984) 550–555, <https://doi.org/10.1007/BF02405364>.
- J. Reyes-Gasga, E.L. Martínez-Piñeiro, E.F. Brès, Crystallographic structure of human tooth enamel by electron microscopy and x-ray diffraction: hexagonal or monoclinic?, *J. Microsc.* 248 (2012) 102–109, <https://doi.org/10.1111/j.1365-2818.2012.03653.x>.
- R.A. Young, P.E. Mackie, Crystallography of human tooth enamel: Initial structure refinement, *Mater. Res. Bull.* 15 (1980) 17–29, [https://doi.org/10.1016/0025-5408\(80\)90155-5](https://doi.org/10.1016/0025-5408(80)90155-5).
- A. La Fontaine et al., Atomic-scale compositional mapping reveals Mg-rich amorphous calcium phosphate in human dental enamel, *Sci. Adv.* 2 (2016), <https://doi.org/10.1126/sciadv.1601145> e1601145.
- G.D. Kamenov, E.M. Lofaro, G. Goad, J. Krigbaum, Trace elements in modern and archaeological human teeth: implications for human metal exposure and enamel diagenetic changes, *J. Archaeol. Sci.* 99 (2018) 27–34, <https://doi.org/10.1016/j.jas.2018.09.002>.
- F. Yun et al., Nanoscale pathways for human tooth decay – central planar defect, organic-rich precipitate and high-angle grain boundary, *Biomaterials* 235 (2020), <https://doi.org/10.1016/j.biomaterials.2019.119748> 119748.
- K.A. DeRocher et al., Chemical gradients in human enamel crystallites, *Nature* 583 (2020) 66–71, <https://doi.org/10.1038/s41586-020-2433-3>.
- R.Z. LeGeros, T. Sakae, C. Bautista, M. Retino, J.P. LeGeros, Magnesium and carbonate in enamel and synthetic apatites, *Adv. Dental Res.* 10 (1996) 225–231, <https://doi.org/10.1177/08959374960100021801>.
- J.C. Elliott, D.W. Holcomb, R.A. Young, Infrared determination of the degree of substitution of hydroxyl by carbonate ions in human dental enamel, *Calcif. Tissue Int.* 37 (1985) 372–375, <https://doi.org/10.1007/BF02553704>.
- S. Risnes, C. Li, On the method of revealing enamel structure by acid etching. Aspects of optimization and interpretation, *Microsc. Res. Tech.* 82 (2019) 1668–1680, <https://doi.org/10.1002/jemt.23333>.
- S. Risnes, M. Saeed, A. Sehic, Scanning electron microscopy (SEM) methods for dental enamel, in: Petros Papagerakis (Ed.), *Odontogenesis: Methods and Protocols*, Ch. 27, Springer, New York, 2019, 293–308.
- F.-Z. Cui, J. Ge, New observations of the hierarchical structure of human enamel, from nanoscale to microscale, *J. Tissue Eng. Regen. Med.* 1 (2007) 185–191, <https://doi.org/10.1002/term.21>.
- V. Uskoković, M.K. Kim, W. Li, S. Habelitz, Enzymatic Processing of Amelogenin during Continuous Crystallization of Apatite, *J. Mater. Res.* 23 (2008) 3184–3195, <https://doi.org/10.1557/JMR.2008.0387>.
- R.S. Lacruz, S. Habelitz, J.T. Wright, M.L. Paine, Dental enamel formation and implications for oral health and disease, *Physiol. Rev.* 97 (2017) 939–993, <https://doi.org/10.1152/physrev.00030.2016>.
- A.H. Meckel, W.J. Griebstein, R.J. Neal, Structure of mature human dental enamel as observed by electron microscopy, *Arch. Oral Biol.* 10 (1965) 775–783.
- D.F.G. Poole, A.W. Brooks, The arrangement of crystallites in enamel prisms, *Arch. Oral Biol.* 5 (1961) 14–IN15, [https://doi.org/10.1016/0003-9969\(61\)90110-8](https://doi.org/10.1016/0003-9969(61)90110-8).
- D. Bajaj, D.D. Arola, On the R-curve behavior of human tooth enamel, *Biomaterials* 30 (2009) 4037–4046, <https://doi.org/10.1016/j.biomaterials.2009.04.017>.
- E. Beniash et al., The hidden structure of human enamel, *Nat. Commun.* 10 (2019) 4383, <https://doi.org/10.1038/s41467-019-12185-7>.
- J. Ge, F.Z. Cui, X.M. Wang, H.L. Feng, Property variations in the prism and the organic sheath within enamel by nanoindentation, *Biomaterials* 26 (2005) 3333–3339, <https://doi.org/10.1016/j.biomaterials.2004.07.059>.
- L.H. He, M.V. Swain, Understanding the mechanical behaviour of human enamel from its structural and compositional characteristics, *J. Mech. Behav. Biomed. Mater.* 1 (2008) 18–29, <https://doi.org/10.1016/j.jmbbm.2007.05.001>.
- J.D. Haines, Physical Properties of Human tooth enamel and enamel sheath material under load, *J. Biomech.* 1 (1968) 117–125.
- O. Duverger, E. Beniash, M.I. Morasso, Keratins as components of the enamel organic matrix, *Matrix Biol.* 52–54 (2016) 260–265, <https://doi.org/10.1016/j.matbio.2015.12.007>.
- C.D. Lynch, V.R. O'Sullivan, P. Dockery, C.T. McGillycuddy, A.J. Sloan, Hunter-Schreger Band patterns in human tooth enamel, *J. Anat.* 217 (2010) 106–115, <https://doi.org/10.1111/j.1469-7580.2010.01255.x>.
- R.A. Harper et al., Acid-induced demineralisation of human enamel as a function of time and pH observed using X-ray and polarised light imaging, *Acta Biomater.* 120 (2021) 240–248, <https://doi.org/10.1016/j.actbio.2020.04.045>.
- T.T.Y. Huang, L.-H. He, M.A. Darendeliler, M.V. Swain, Correlation of mineral density and elastic modulus of natural enamel white spot lesions using X-ray microtomography and nanoindentation, *Acta Biomater.* 6 (2010) 4553–4559, <https://doi.org/10.1016/j.actbio.2010.06.028>.
- L.M. Silverstone, C.A. Saxton, I.L. Dogon, O. Fejerskov, Variation in the pattern of acid etching of human dental enamel examined by scanning electron microscopy, *Caries Res.* 9 (1975) 373–387, <https://doi.org/10.1159/000260179>.
- K.A. Galil, G.Z. Wright, Acid etching patterns on buccal surfaces of permanent teeth, *Pediatr. Dent.* 1 (1979) 230–234.
- O. Fejerskov, B. Nyvad, E.A.M. Kidd, Clinical appearances of caries lesions, in: O. Fejerskov, Edwina A.M. Kidd (Eds.), *Dental Caries the Disease and Its Clinical Management*, Ch. 2, 2008, 7–18.
- G.E. Tiznado-Orozco, R. García-García, J. Reyes-Gasga, Structural and thermal behaviour of carious and sound powders of human tooth enamel and dentine, *J. Phys. D Appl. Phys.* 42 (2009), <https://doi.org/10.1088/0022-3727/42/23/235408> 235408.
- X. Li, D. Pan, S. Lin, Z. Zhuang, Z. Lin, Facile *in vitro* hydroxyapatite remineralization of human enamel with remarkable hardness, *CrystEngComm* 15 (2013) 4351–4356, <https://doi.org/10.1039/C3CE26947G>.
- T. Buchwald, Z. Buchwald, Assessment of the Raman spectroscopy effectiveness in determining the early changes in human enamel caused by artificial caries, *Analyst* 144 (2019) 1409–1419, <https://doi.org/10.1039/C8AN01494A>.
- L. Wang et al., A new model for nanoscale enamel dissolution, *J. Phys. Chem. B* 109 (2005) 999–1005, <https://doi.org/10.1021/jp046451d>.
- B.B. Cerci, L.S. Roman, O. Guariza-Filho, E.S. Camargo, O.M. Tanaka, Dental enamel roughness with different acid etching times: Atomic force microscopy study, *Eur. J. General Dentistry* 1 (2012) 187–191, <https://doi.org/10.4103/2278-9626.105385>.
- M. Sorozini, C. dos Reis Perez, G.M. Rocha, Enamel sample preparation for AFM: Influence on roughness and morphology, *Microsc. Res. Technique* 81, 1071–1076, doi:10.1002/jemt.23073 (2018).
- P. Li, et al., Nanoscale characterization of the impact of beverages on the enamel surface of human teeth. arXiv preprint arXiv:1909.02419, 1–17 (2019).
- J.W. Simmelink, V.K. Nygaard, Ultrastructure of striations in carious human enamel, *Caries Res.* 16 (1982) 179–188, <https://doi.org/10.1159/000260595>.
- E. Salvati et al., Finite element modelling and experimental validation of enamel demineralisation at the rod level, *J. Adv. Res.* 29 (2021) 167–177, <https://doi.org/10.1016/j.jare.2020.08.018>.
- O. Ilie, A.G. van Turnhout, M.C.M. van Loosdrecht, C. Picioreanu, Numerical modelling of tooth enamel subsurface lesion formation induced by dental plaque, *Caries Res.* 48 (2014) 73–89, <https://doi.org/10.1159/000354123>.
- T. Sui et al., *In situ* monitoring and analysis of enamel demineralisation using synchrotron X-ray scattering, *Acta Biomater.* 77 (2018) 333–341, <https://doi.org/10.1016/j.actbio.2018.07.027>.
- S. Siddiqui, P. Anderson, M. Al-Jawad, Recovery of crystallographic texture in remineralized dental enamel, *PLoS ONE* 9 (2014), <https://doi.org/10.1371/journal.pone.0108879> e108879.
- R. Free, K. DeRocher, R. Xu, D. Joester, S.R. Stock, A method for mapping submicron-scale crystallographic order/disorder applied to human tooth enamel, *Powder Diff.* 35 (2020) 117–123, <https://doi.org/10.1017/S0885715620000251>.

- [52] T. Sui, S. Ying, A.M. Korsunsky, G. Landini, X-ray study of human dental tissues affected by erythroblastosis fetalis, *J. Dent. Res.* 94 (2015) 1004–1010, <https://doi.org/10.1177/0022034515580987>.
- [53] M.C. Dean, K.M. Spiers, J. Garrevoet, A. Le Cabec, Synchrotron X-ray fluorescence mapping of Ca, Sr and Zn at the neonatal line in human deciduous teeth reflects changing perinatal physiology, *Arch. Oral Biol.* 104 (2019) 90–102, <https://doi.org/10.1016/j.archoralbio.2019.05.024>.
- [54] K.J.S. Sawhney et al., A test beamline on Diamond Light Source, *AIP Conf. Proc.* 1234 (2010) 387–390, <https://doi.org/10.1063/1.3463220>.
- [55] P. Kirkpatrick, A.V. Baez, Formation of optical images by X-rays, *J. Opt. Soc. Am.* 38 (1948) 766–774, <https://doi.org/10.1364/JOSA.38.000766>.
- [56] K. Momma, F. Izumi, VESTA 3 for three-dimensional visualization of crystal, volumetric and morphology data, *J. Appl. Crystallogr.* 44 (2011) 1272–1276, <https://doi.org/10.1107/S0021889811038970>.
- [57] J.M. Hughes, M. Cameron, D.C. Kevin, Structural variations in natural F, OH, and Cl apatites, *Am. Mineral.* 74 (1989) 870–876.
- [58] W.H. Bragg, W.L. Bragg, The reflection of X-rays by crystals, *Proc. Roy. Soc. London. Series A, Containing Papers of a Mathematical and Physical Character* 88, 428–438, doi:doi:10.1098/rspa.1913.0040 (1913).
- [59] M.E. Fitzpatrick, et al., Determination of residual stresses by X-ray diffraction, 2005.
- [60] W.S. Rasband, ImageJ, U. S. National Institutes of Health, Bethesda, Maryland, USA, <https://imagej.nih.gov/ij/>. (1997–2018).
- [61] J. Schindelin et al., Fiji: an open-source platform for biological-image analysis, *Nat. Methods* 9 (2012) 676, <https://doi.org/10.1038/nmeth.2019>.
- [62] M. Basham et al., Data Analysis Workbench (DAWN), *J. Synchrotron Radiation* 22 (2015) 853–858, <https://doi.org/10.1107/S1600577515002283>.
- [63] J. Filik et al., Processing two-dimensional X-ray diffraction and small-angle scattering data in DAWN 2, *J. Appl. Crystallogr.* 50 (2017) 959–966, <https://doi.org/10.1107/S1600576717004708>.
- [64] A.C. Deymier-Black, J.D. Almer, S.R. Stock, D.R. Haeffner, D.C. Dunand, Synchrotron X-ray diffraction study of load partitioning during elastic deformation of bovine dentin, *Acta Biomater.* 6 (2010) 2172–2180, <https://doi.org/10.1016/j.actbio.2009.11.017>.
- [65] T. Sui et al., *In situ* X-ray scattering evaluation of heat-induced ultrastructural changes in dental tissues and synthetic hydroxyapatite, *J. R. Soc. Interface* 11 (2014) 20130928, <https://doi.org/10.1098/rsif.2013.0928>.
- [66] S. Gražulis et al., Crystallography Open Database (COD): an open-access collection of crystal structures and platform for world-wide collaboration, *Nucleic Acids Res.* 40 (2012) D420–D427, <https://doi.org/10.1093/nar/gkr900>.
- [67] D. Zagorac, H. Muller, S. Ruehl, J. Zagorac, S. Rehme, Recent developments in the Inorganic Crystal Structure Database: theoretical crystal structure data and related features, *J. Appl. Crystallogr.* 52 (2019) 918–925, <https://doi.org/10.1107/S160057671900997X>.
- [68] M. Al-Mosawi et al., Crystallographic texture and mineral concentration quantification of developing and mature human incisal enamel, *Sci. Rep.* 8 (2018) 14449, <https://doi.org/10.1038/s41598-018-32425-y>.
- [69] I.-M. Low, Depth-profiling of crystal structure, texture, and microhardness in a functionally graded tooth enamel, *J. Am. Ceram. Soc.* 87 (2004) 2125–2131, <https://doi.org/10.1111/j.1151-2916.2004.tb06369.x>.
- [70] P. Seredin et al., Local study of fissure caries by Fourier transform infrared microscopy and X-ray diffraction using synchrotron radiation, *J. Synchrotron Radiation* 20 (2013) 705–710, <https://doi.org/10.1107/S0909049513019444>.
- [71] T. Scientific, User's guide Avizo software 2019, 2019.
- [72] A. Thompson, et al., X-ray data booklet, 2009.
- [73] D. Drouin et al., CASINO V2.42: a fast and easy-to-use modeling tool for scanning electron microscopy and microanalysis users, *Scanning* 29 (2007) 92–101, <https://doi.org/10.1002/sca.20000>.
- [74] N.J. Cochrane et al., An X-ray microtomographic study of natural white-spot enamel lesions, *J. Dent. Res.* 91 (2012) 185–191, <https://doi.org/10.1177/0022034511429570>.
- [75] M. Raza et al., Comparison of demineralization around orthodontic brackets cured by conventional method and transillumination technique—an *in vitro* evaluation 16–16, *J. Orthodontic Sci.* 9 (2020), https://doi.org/10.4103/jos.jos_3_20.
- [76] R.C.G. De Medeiros, J.D. Soares, F.B. De Sousa, Natural enamel caries in polarized light microscopy: differences in histopathological features derived from a qualitative versus a quantitative approach to interpret enamel birefringence, *J. Microsc.* 246 (2012) 177–189, <https://doi.org/10.1111/j.1365-2818.2012.03609.x>.
- [77] N.I. Kato, Y. Kohno, H. Saka, Side-wall damage in a transmission electron microscopy specimen of crystalline Si prepared by focused ion beam etching, *J. Vac. Sci. Technol.*, A 17 (1999) 1201–1204, <https://doi.org/10.1116/1.581795>.
- [78] M. Rommel et al., Comprehensive study of focused ion beam induced lateral damage in silicon by scanning probe microscopy techniques, *J. Vac. Sci. Technol.*, B 28 (2010) 595–607, <https://doi.org/10.1116/1.3431085>.
- [79] T. Kodaka, T. Sano, Energy-dispersive X-Ray microanalysis of the artificial caries-like lesion of human enamel embedded with and without polyester resin, *J. Showa Univ. Dental Soc.* 22 (2002) 339–344.
- [80] M.D. de Marsillac, R. de Sousa Vieira, Assessment of artificial caries lesions through scanning electron microscopy and cross-sectional microhardness test, *Indian J. Dental Res.* 24, 249–254, doi:10.4103/0970-9290.116699 (2013).
- [81] A. Ortiz, M. Briano, M. Esparza, J. Juárez, Comparison of chemical elements on carious & normal premolar's enamel layers using energy dispersive X ray spectrometer (X Ray-EDS), *Microsc. Res. Tech.* 2 (2014) 81–91.
- [82] L. Raue, H. Klein, Calculation of anisotropic properties of dental enamel from synchrotron data, *J. Synchrotron Radiation* 18 (2011) 550–556, <https://doi.org/10.1107/S0909049511011071>.
- [83] V. Latza et al., Multi-scale thermal stability of a hard thermoplastic protein-based material, *Nat. Commun.* 6 (2015) 8313, <https://doi.org/10.1038/ncomms9313>.
- [84] Y. Yang et al., Salivary acquired pellicle-inspired DpSpSEKC peptide for the restoration of demineralized tooth enamel, *Biomed. Mater.* 12 (2017), <https://doi.org/10.1088/1748-605X/aa5daf.025007>.
- [85] H. Deyhle, S.N. White, O. Bunk, F. Beckmann, B. Müller, Nanostructure of carious tooth enamel lesion, *Acta Biomater.* 10 (2014) 355–364, <https://doi.org/10.1016/j.actbio.2013.08.024>.